JOURNAL OF PROPULSION AND POWER
Vol. 27, No. 1, January–February 2011

Numerical Investigation of Inlet Distortion on a Wing-Embedded Lift Fan

Nicolas Thouault,[*] Christian Breitsamter,[†] and Nikolaus A. Adams[‡]
Technische Universität München, 85747 Garching, Germany

DOI: 10.2514/1.46046

The inlet distortion arising on a generic fan-in-wing wind-tunnel model is investigated by means of unsteady Reynolds-averaged Navier–Stokes simulations. Flow separation occurs on the inlet lip and generates a separation bubble above the rotor blades. A distortion of the total pressure distribution at the fan inlet significantly influences the blade loading. The strong flow-velocity gradient over the inlet lip induces an increase of the axial-velocity magnitude, resulting in a reduction of incidence angle on the rotor blade. In the bubble-core region, the low axial-velocity magnitude enhances the blade incidence angle and provokes blade tip stall. Steady-state calculations, using an actuator disk approach, are also conducted to identify the key parameters affecting lip boundary-layer separation. The ratio of freestream velocity to fan jet velocity and the inlet-lip radius affect the total pressure distribution by modifying the location of the flow separation. The angle of attack on the wing has a negligible impact on the inlet distortion. An inlet lip with a large radius at its front part suppresses the lip separation and considerably reduces the total pressure distortion. Injecting a jet over the inlet lip can be a solution to actively control the lip flow.

Nomenclature

C_p = mean (time-averaged) pressure coefficient
C_T = mean thrust coefficient, $T/(\rho_\infty n^2 D^4)$
C_μ = momentum coefficient, $\dot{m}_s U_s/(0.5\rho_\infty U_\infty^2 S)$
c = root chord, m
D = fan diameter, m
$l_{\max}$ = maximum radial length of the lip separation bubble, m
M = mean fan torque, N · m
$\dot{m}_s$ = slot jet mass-flow rate, kg/s
N = fan rotational speed, rpm
n = fan rotational speed, rps
P_S = mean static pressure, Pa
$P_{S\infty}$ = freestream mean static pressure, Pa
P_T = mean total pressure, Pa
$P_{T\infty}$ = freestream mean total pressure, Pa
Q = mean volumetric flow rate through the fan, m^3/s
R = fan radius, m
Re_c = Reynolds number based on the root chord
r = radial position, m
r_{lip} = inlet-lip radius, m
S = wing planform, m^2
s = wing span, m
T = mean fan thrust, N
t = wing maximum thickness, m
U_j = jet velocity, m/s
U_s = velocity of the jet exiting the blowing slot, m/s
U_t = blade tip speed, m/s
U_∞ = freestream velocity, m/s
v_a, v_c, v_r = axial, circumferential, and radial velocity, m/s
$\bar{v}_a$, $\bar{v}_c$, $\bar{v}_r$ = axial, circumferential, and radial mean velocity, m/s
v'_a, v'_c, v'_r = fluctuation part of v_a, v_c, v_r, m/s
x, y, z = streamwise, spanwise, and vertical coordinate directions, m
y^+ = nondimensional wall distance
α = angle of attack, deg
γ = swirl angle, deg
$\bar{\gamma}$ = mean swirl angle, deg
ϕ = flow coefficient, $Q/(nD^3)$
θ = angular position around the fan, deg
ρ_∞ = freestream density, $\mathrm{kg/m}^3$
ψ = pressure-rise coefficient, $\Delta P_S/(\rho_\infty n^2 D^2)$
τ = torque coefficient, $M/(\rho_\infty n^2 D^5)$

I. Introduction

VERTICAL and short takeoff and landing (V/STOL) aircraft can be an alternative for short- to medium-range aircraft, to relieve congestion on airports and to face the increase in air transportation traffic [1]. The lift fan is a potential solution to provide elevated lift for V/STOL capability [2]. For example, a lift fan was contained in the wing of the Ryan XV-5 fan-in-wing NASA experimental aircraft to offer hovering ability. A lift fan is also currently used in the F-35B fuselage for longitudinal stability purposes and to provide additional lift.

A large amount of experimental and numerical investigations have been undertaken to study the effects of inlet distortion on the performance of axial compressors. Nonuniform inflow can induce compressor stall or surge, resulting in a significant drop of efficiency. Vibrations can also be induced by distortion on a fan [3]. The main sources of distortions, related to each other, are the total pressure, the total temperature, and the swirl distortions [4]. The effect of inlet circumferential distortion in a transonic compressor rotor was studied by Hah et al. [5]. The distortion travels through the rotor blade passage and can affect the stator. Pressure distortion can induce a swirl distortion that is transmitted through the blade passage in multistage fans [6]. Inflow distortion can be generated at the compressor inlet, depending on the installation. For example, the shape of the hub cap [7] or the nacelle droop [8] can be a source of distortion. The nonuniform inflow distribution is a critical issue for fighter aircraft at high angle of attack [9]. Flow separation can occur on the engine intake lip and can strongly affect the inlet total pressure distribution.

For V/STOL aircraft, inflow distortion is also a major problem. For example, a large recirculation area can be generated on the nacelle

---

Received 18 June 2009; revision received 6 July 2010; accepted for publication 24 August 2010.

[*] Research Engineer, Institute of Aerodynamics. Member AIAA.

[†] Chief Scientist, Institute of Aerodynamics. Associate Fellow AIAA.

[‡] Professor, Institute of Aerodynamics. Member AIAA.

droop of a tilt-nacelle aircraft at severe freestream conditions [10]. The inlet distortion is critical for an axial fan installed orthogonally to the freestream direction and can possibly cause an excitation of the fan at its natural frequency and provoke significant damage. On the X-35B under crossflow condition, separation can occur on the bellmouth inlet, considerably affecting the flow angularity and total pressure distribution at the lift-fan inlet section [11]. In this study, the design of the inlet lip is of great interest to reduce the total pressure distortion. For a fan-in-wing configuration in transition flight out-of-ground effect, a nonuniform swirl angle distribution is observed, aggravating the noise level [12]. A rough description of the velocity distribution at the fan inlet is provided in [13]. Regarding cruise performance, the fan has to be housed compactly in the wing. The inflow depth and the inlet-lip shape are parameters influencing the inlet total pressure and swirl distortions [14]. For fan-in-wing configurations, guiding vanes above the fan inlet can improve the flow ingestion [15–18]. An inlet guide vane located near the front part of the inlet lip to control the lip flow was used for various V/STOL applications: for example, a lift fan fitted in a nacelle [19] or an engine mounted in fuselage [20]. However, the inlet guide vane wake impinges on the rotor causing a spatial nonuniform velocity distribution [21]. In related studies, generic fan-in-wing configurations were analyzed by means of experimental investigations and computational fluid dynamics (CFD) simulations. The situation studied reflects a transition flight out-of-ground effect. A generic wind-tunnel model was manufactured and the performance of the wing with various fan arrangements was analyzed experimentally in [22]. Further, a configuration with a single fan located at the rear part of the wing (Fig. 1) has been reproduced numerically, using a sliding-mesh technique to model fan rotation. The fan-in-wing aerodynamic characteristics were documented based on time-averaged unsteady Reynolds-averaged Navier–Stokes (URANS) results in [23]. In addition, the effect of relevant configuration design parameters (e.g., location of the fan in the wing, fan diameter) were reported in [24] using steady-state actuator disk simulations.

As previously stated, distortion due to inlet-lip separation appears in a wide range of V/STOL configurations. However, a number of questions remain open concerning the flow characteristics at the fan inlet, useful for the design of such lift fans. The use of state-of-the-art CFD methods can contribute to provide further information on the flow properties of a lift fan being installed in a wing and can allow a large spectrum of parameter variation. In the present study, a detailed analysis of the inlet distortion will be provided for a particular fan-in-wing configuration of fixed parameters based on URANS simulation results. The aerodynamic characteristics of the lift fan integrated in the wing will be compared to steady results of the fan alone without inlet distortion. Then, using an actuator disk approach to model the fan, the main parameters affecting the inlet total pressure distortion will be documented. A blown-lip solution will be investigated with a view to suppress the lip flow separation. Sections II and III are complementary to provide an extensive study of the lift-fan inlet distortion in order to increase the design sensitivity.

II. Lift-Fan Inlet Distortion

Using URANS results of the entire generic wind-tunnel model geometry, the aerodynamic characteristics of the inlet distortion are studied in detail by comparison with a simulation of the fan without inlet distortion.

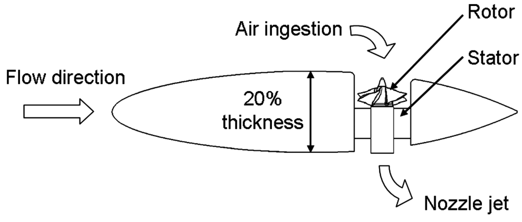

Fig. 1 Schematic view of the experimental setup.

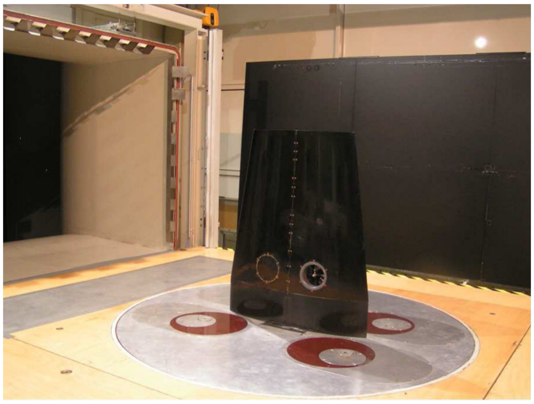

Fig. 2 Model set up in wind-tunnel test section.

A. Wind-Tunnel Model

A NACA 16-020 type of airfoil is used. The generic semispan model (Fig. 2) has an aspect ratio of 2.3, a semispan area of $S = 0.683\ \mathrm{m}^2$, a taper ratio of 0.71, and 0° sweep of the 50% root chord line. The rear fan axis is located at $x = \frac{2}{3}c$ and at $y = 0.12b$ from the root chord. The fan has a diameter of $D = 0.13c$. The model is installed on a peniche to raise the wing out of the wind-tunnel wall boundary layer. The model fan is composed of two stages: a four-bladed rotor and a four-bladed stator. The engine is located inside the stator and therefore gives a realistic configuration with no external device around the wing. The cables to provide power and to measure

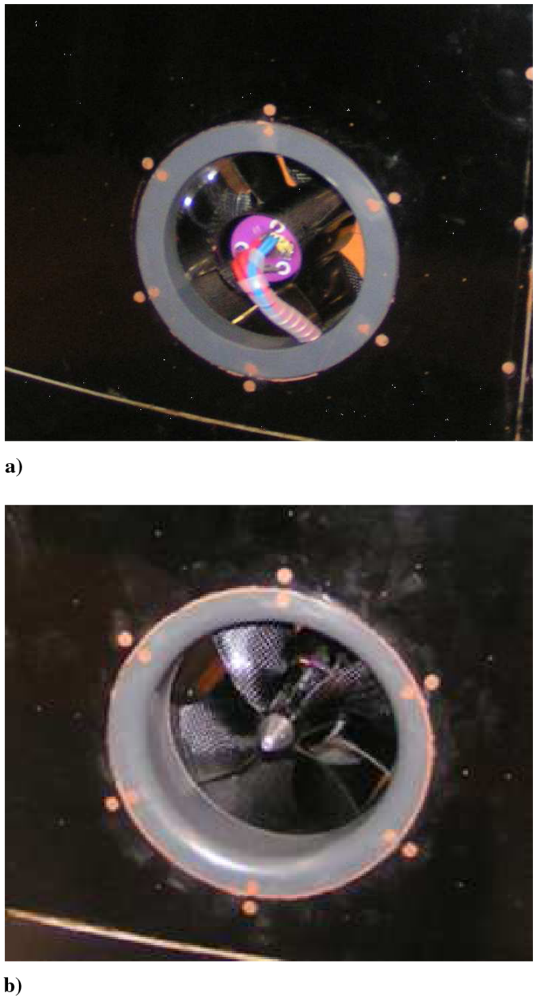

Fig. 3 Model details: a) fan exit and b) inlet section.

Table 1 Fan geometry details

Parameter	Value
D/c	0.13
r_{lip}/D	0.083
Hub-tip ratio	0.42
Rotor blade aspect ratio	0.95
Solidity at hub/tip (rotor)	1.1/0.43
Stagger angle at hub/tip (rotor)	15°/70°
Tip clearance ($\%D$)	1

the engine temperature are fixed behind one stator blade trailing edge (Fig. 3a) to minimize their influence. On the wing upper side, a constant lip radius-to-diameter ratio of $r_{\mathrm{lip}}/D = 0.083$ (Fig. 3b) was used during all the tests. Details of the fan geometry are listed in Table 1. The cylindrical coordinate system used is presented in Fig. 4.

A variety of experimental techniques were carried out to provide a reliable database for simulation validation. The experimental work has been performed in the Göttingen-type wind tunnel A at the Institute of Aerodynamics, Technische Universität München. Different types of tests have been carried out including force, surface pressure measurements, flowfield mapping using stereo particle image velocimetry (PIV) near the trailing edge, and wool-tuft flow visualization. Details of the tests conducted with the corresponding results can be found in [22].

B. CFD Simulations Setup

The flow simulation software ANSYS CFX is used to perform URANS simulations of this fan-in-wing configuration as well as steady simulations of the fan alone without inlet distortion.

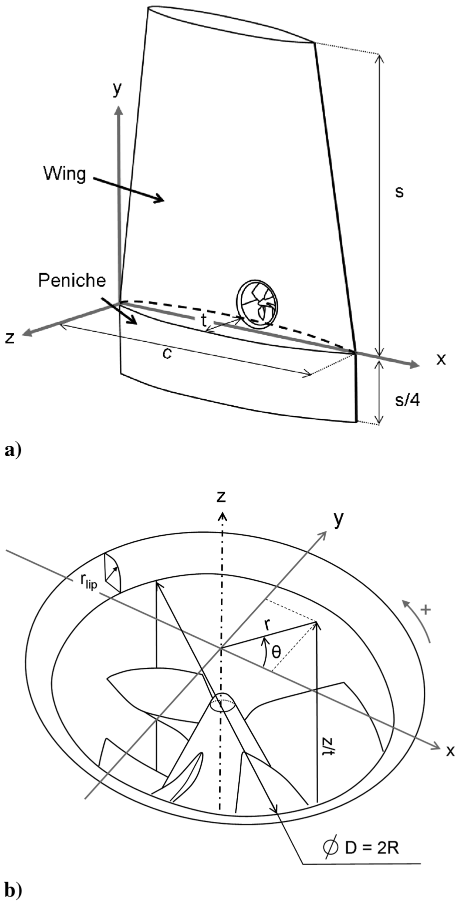

a)

b)

Fig. 4 Sketch of the a) wind-tunnel model and b) fan inlet geometrical parameters.

1. Fan-in-Wing Computations

In this section, the numerical method of the URANS fan-in-wing simulation is described. In [23], the accuracy of the numerical results has been carefully assessed and validated against a wide range of experimental data. It has been found that the numerical simulation provides a good prediction of the time-averaged velocity distribution by comparison with stereo-PIV measurements performed in the trailing-edge vicinity. In addition, a fair agreement has been obtained for the time-averaged aerodynamic coefficients (lift, drag, and pitching moment) with respect to the complexity of the flowfield and of the geometry. Time-averaged chordwise pressure distributions and surface streamlines on the wing are well predicted by the URANS simulation. In this paper, circumferential distributions of the time-averaged pressure coefficient around the fan inlet are shown in Fig. 5 as an example. The time-averaged pressure distribution around the fan inlet lip is well represented by the URANS simulation.

a. Numerical Method. A structured mesh of 4×10^6 nodes is generated around the geometry with ICEM CFD. The influence of the wires providing power (Fig. 3a) to the engine is neglected in the numerical simulation. The fan geometry is simplified to create a suitable blocking around the geometry. The gaps between the rotor and stator and the holes are removed. The rotor blade filets are also neglected. Thus, the blade geometry in the hub vicinity is extrapolated. Despite these changes, the geometry is precisely modeled,

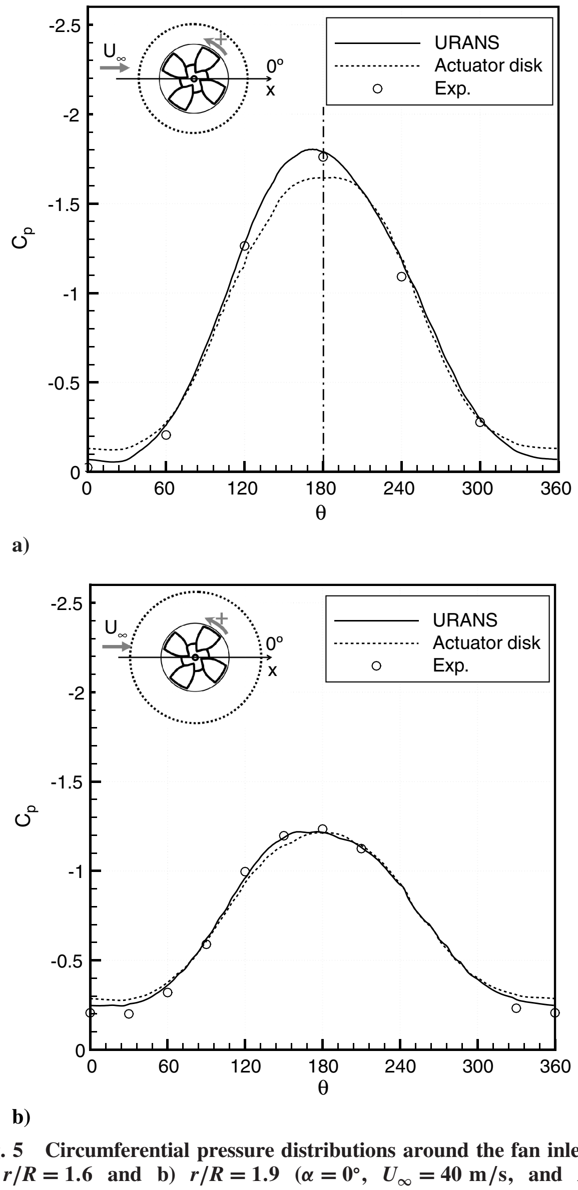

a)

b)

Fig. 5 Circumferential pressure distributions around the fan inlet at a) $r/R = 1.6$ and b) $r/R = 1.9$ ($\alpha = 0°$, $U_\infty = 40$ m/s, and $N = 26,200$ rpm).

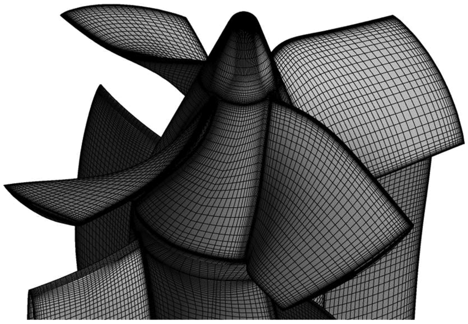

Fig. 6 Surface mesh on the rotor blades and hub.

including the tip clearance. An O-grid is set around the rotor blade to handle the tip clearance with 20 nodes across the gap. The surface mesh on the rotor blades is presented in Fig. 6.

A second-order discretization of the convective terms is used throughout all calculations. The total-energy model is used to account for compressibility effects, which are particularly significant at the blade tip and on the inlet lip. This model introduces a transport equation for the total enthalpy [25]. The *k*-ω shear stress transport (SST) model from Menter [26] is used for all computations. The rotation of the fan is modeled using a sliding-mesh approach. A periodicity of the fan coefficients is achieved after four revolutions. The results are time-averaged over a fan period after five computed revolutions. A time history of the thrust and torque coefficients is given in Sec. II.C.2. Additional information (e.g. nodes distribution, grid-dependence study) can be found in [23].

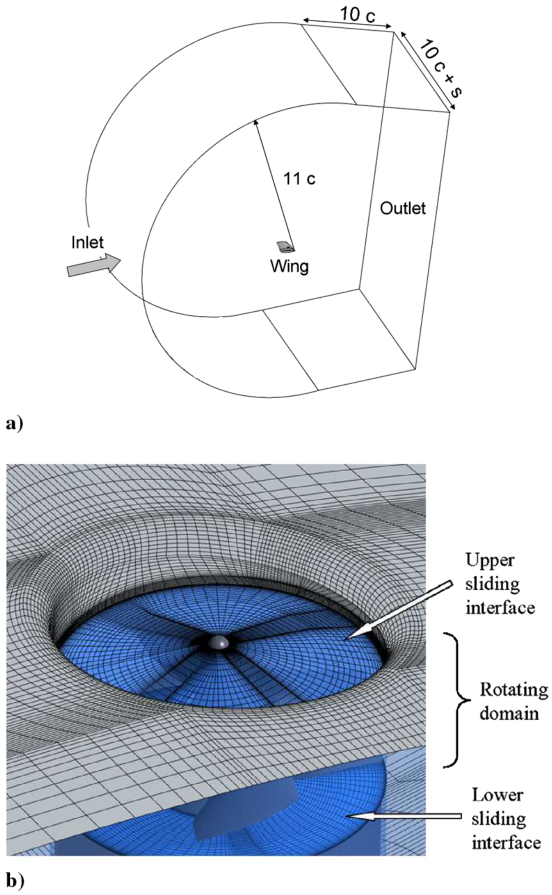

Fig. 7 Sketch of the a) computational domain and the b) rotating domain for the fan-in-wing computations.

b. Boundary Conditions. The overall computational domain is a C-H topology (Fig. 7a). Ten chords were used in each direction from the wing to create the computational domain. At the domain inlet, an uniform velocity profile is applied. The inlet turbulence intensity level is set to 0.4% accordingly to the wind-tunnel data. Free-slip wall boundary conditions are imposed on the lateral sides of the domain. The temperature and pressure of reference were set accordingly to the experiment, respectively, 298 K and $P_{S\infty} = 0.96 \times 10^5$ Pa. An opening boundary condition [25] is placed at the domain outlet with a reference relative pressure of $P_S - P_{S\infty} = 0$ Pa averaged over the entire outlet surface. An opening boundary condition with a uniform velocity profile is applied on the top and bottom of the domain. This last boundary condition is similar to the inlet of the computational domain. The peniche is included in the computational domain and a free-slip condition is placed at its root chord. No boundary-layer mesh is thus generated on the wind-tunnel floor, consequently reducing the computational costs.

For the unsteady calculation, the area surrounding the blades is designated as sliding mesh. Sliding interfaces separate the rotating domain from the stationary domain (Fig. 7b) which accounts for the interaction between the rotor and the stator. The treatment of the interface fluxes is fully implicit and fully conservative. In the rotating domain, the shroud is set as a so-called counter-rotating wall [25]. Therefore, the shroud is stationary with respect to stationary frame.

2. *Simulations of the Fan Alone Without Inlet Distortion*

As reference, steady-state simulations of the fan without inlet distortion are carried out.

a. Numerical Details. Only one blade passage is simulated and periodic conditions are imposed on the sides of the domain to reduce the computational resource requirements. The computational domain is presented in Fig. 8. An inlet mass-flow condition is imposed in the fan axial direction. The flow coefficient, $\phi = 0.87$, is an input from the fan-in-wing time-averaged URANS simulation results (for $U_\infty = 40$ m/s, $N = 26,200$ rpm and $\alpha = 0°$). As shown in Fig. 8, the hub is extended up to the domain outlet, for simplicity. A reference relative pressure of $P_S - P_{S\infty} = 0$ Pa is set at the domain outlet. This reference pressure is averaged over the entire outlet surface. Details of the grids employed are provided in the next section. The *k*-ω SST turbulence model and a second-order discretization scheme are used for all fan-alone simulations. The same flow properties (e.g., reference pressure, freestream temperature, and density) are employed as the URANS fan-in-wing simulations. A turbulence intensity of 1% is prescribed at the inlet of the computational domain.

Stage interfaces are used to separate the rotating domain surrounding the rotor blade to the rest of the fluid domain. The stage interfaces average circumferentially the information transferring between the different reference frames and consequently provide a

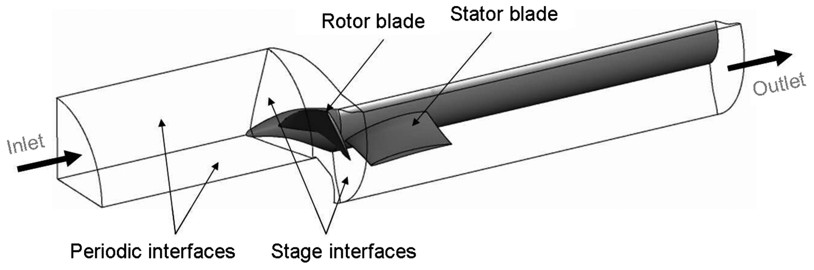

Fig. 8 Computational domain of the fan-alone simulations.

Table 2 Details of the grids employed for the simulations of the fan under ideal flow conditions

Parameter (rotor/stator)	Coarse	Medium	Fine
Normal layers	33/30	38/32	46/38
Spanwise layers	55/38	64/44	78/56
Circumferential points	104/128	120/144	148/164
Leading-edge spacing/chord ($\times 10^{-3}$)	1.5/1.9	1.3/1.6	1.1/1.4
Total number of nodes ($\times 10^{6}$)	0.42	0.62	1.1

Table 3 Comparison of fan coefficients for various grid levels

Parameter	Coarse	Medium	Fine
ψ	0.795	0.811	0.827
τ	0.0102	0.0103	0.0103
C_T	0.339	0.343	0.347

steady-state solution in each reference frame [25]. The total-energy model is also used. All maximum residuals (turbulence, heat transfer, and momentum quantities) are converged here to less than 10^{-4}. A converged solution is obtained in approximately 40 CPU hours for the medium grid of Table 2. Two processors on a 12-node Altix cluster are used to carry out the fan-alone simulations.

b. Grid-Dependence Study. Three different meshes are tested: a coarse grid of 4.2×10^5 nodes, a medium grid (with the same nodes distribution as in the fan-in-wing simulation) of 6.2×10^5 nodes, and a fine grid of 1.1×10^6 nodes. Relevant dimensions of the grids are given in Table 2. The flow coefficient is $\phi = 0.87$ for all simulations. The solver performs an automatic near-wall treatment as the mesh is refined. To benefit from a near-wall formulation, the nondimensional wall distance y^+ remains constant (less than 1) on the rotor and stator blades for all grids.

The relative difference between the fine and medium grids is about 1% for the pressure-rise and thrust coefficients (Table 3). The pressure distribution on the blade is relatively complex, but a graphical observation (not presented in this paper) can give some insight on the impact of grid refinement on the fan coefficients. Slight lower pressure is predicted on the upper side of the blade for the fine grid, especially near the blade tip. An evaluation of the pressure distribution also indicates that higher pressure on the blade lower side and on the front part of the blade near the tip for the fine grid. For this reason, higher thrust and pressure-rise coefficients are predicted with the fine grid. A mesh refinement has a negligible effect on the prediction of the torque coefficient τ. A relatively coarse mesh can be a good approximation of the pressure-rise coefficient ψ, as well as of the thrust coefficient C_T, and can therefore be sufficient for achieving a URANS fan-in-wing calculation. Indeed, if the focus is on the wing aerodynamic behavior, a coarse fan grid can give a satisfying prediction of the wing loading at lower computational cost. Note that the pressure rise ΔP_S is defined here as the pressure difference between the fan exit (area-averaged at $z/t = -0.37$) and the fan inlet (area-averaged at $z/t = 0.33$).

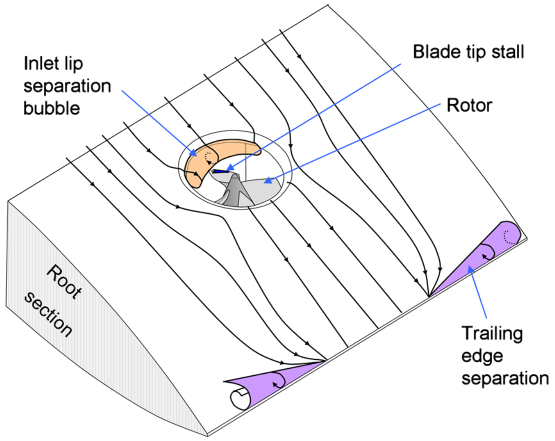

Fig. 9 Sketch of the flow topology on the wing upper side ($\alpha = 0°$).

C. Inlet Distortion Characteristics

In this section, the inflow distortion of the fan-in-wing wind-tunnel model is studied. In particular, velocity components obtained in the URANS fan-in-wing simulation are compared to the reference case (fan alone) to precisely document the properties of this generic inlet distortion configuration. The angle of attack is $\alpha = 0°$; the freestream velocity is $U_\infty = 40$ m/s, corresponding to $Re_c = 2 \times 10^6$; and the fan rotational speed is $N = 26,200$ rpm.

1. Blade Dynamic Loading

The fan flow has a strong influence on the flow topology of the wing upper side (Fig. 9). Boundary-layer separation occurs on the inlet lip and generates a separation bubble above the rotor blades. Figure 10a shows the total pressure ratio distribution in a fan cross section located at $z/t = 0.37$ (Fig. 10b). The fan rotates counterclockwise, as seen from above. The core of the separation bubble can clearly be identified by a region of low total pressure ratio in the range of $0.90 \leq P_T/P_{T\infty} \leq 0.96$. For this fan-in-wing configuration, the major part of the inlet distortion originates from inlet-lip flow separation. Thus, the total pressure distortion is localized in the front part of the fan inlet. A retreating and advancing flow condition on the rotor blades is responsible for the asymmetric shape of the total pressure distribution with respect to the line $\theta = 0°$.

The time dependency of the flow, initiated by the fan rotation, induces a significant unsteady behavior of the total pressure distortion at the fan inlet. Reverse flow, characterized by a positive axial-velocity component (see Sec. II.C.2), is observed near the front part of the shroud. Figure 11a shows an isosurface of static pressure ratio at different times separated by approximately 2 μs. It represents

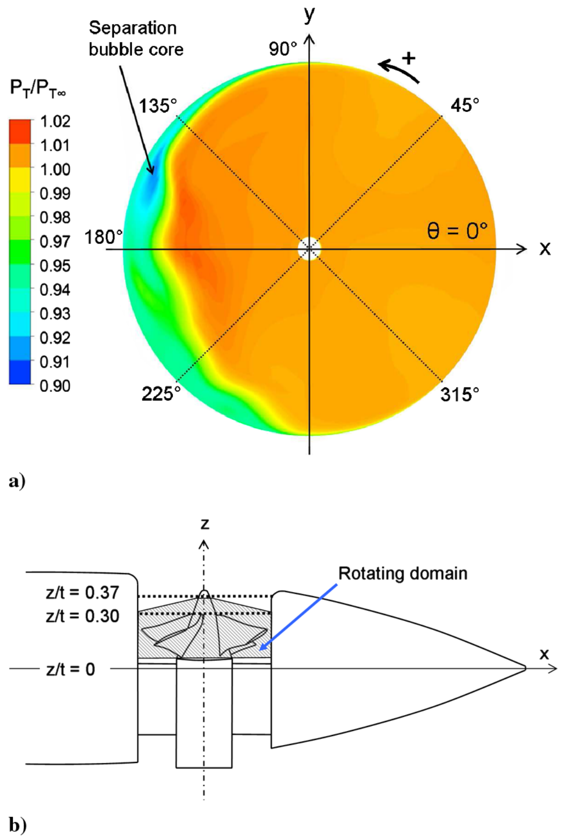

Fig. 10 Inflow distortion characteristics: a) mean total pressure ratio distribution $P_T/P_{T\infty}$ at $z/t = 0.37$ and b) location of the investigated fan inlet cross sections ($U_\infty = 40$ m/s, $N = 26,200$ rpm, and $\alpha = 0°$).

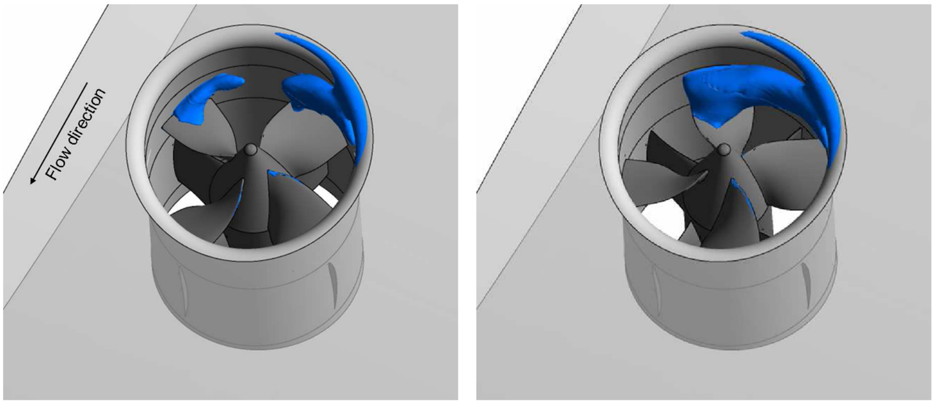

a) b)

Fig. 11 Isosurfaces of static pressure ratio $P_S/P_{S\infty} = 0.92$ at the fan inlet section at different times ($U_\infty = 40$ m/s, $N = 26,200$ rpm, and $\alpha = 0°$).

the core of the separation bubble and gives some insight into its dynamic characteristics. The flow tends to separate on the side of the inlet lip closer to the advancing blade (Fig. 11a). A separation bubble is generated at this location and impinges on the advancing blade. The bubble is stretched, due to the rotating rotor blade, and its circumferential extension is increased (Fig. 11b). As the rotor blade begins to retreat, the bubble is split into two separate parts. One part is conveyed by the retreating blade and progressively disappears from the blade upper side. The other part remains attached on the advancing blade.

The rotor blade experiences tip stall when the blade begins to retreat (Fig. 12). The stall region depends also on the advancing and retreating flow condition because of its asymmetric behavior and corresponds approximately to the location of low static pressure ratio $P_S/P_{S\infty}$ identified in Fig. 10a. The tip-stall region is linked to the recirculation area provoked by the flow separation on the inlet lip. The stall area as well as the separation bubble show a dynamic behavior, due to the fan rotation.

A dynamic loading on the fan is therefore induced by the inlet total pressure distortion. The fan dynamic loading is evident from the significant time variations of the thrust and torque coefficients (Fig. 13). The mean values are $C_T = 0.47$ and $\tau = 0.017$. Note that both thrust and torque coefficients are periodically over a quarter-revolution.

2. *Velocity Distribution at the Fan Inlet*

Nondimensionalized mean axial $\bar{v}_a/U_t$, circumferential $\bar{v}_c/U_t$, and radial $\bar{v}_r/U_t$ velocity distributions at the fan inlet are shown in Fig. 14 in a fan cross section located at $z/t = 0.37$ (Fig. 10b). Recall that the cylindrical coordinate system used is sketched in Fig. 4b. In the front part of the fan inlet ($90° \le \theta \le 270°$), time-averaged axial velocities of significant magnitude are observed (Fig. 14a).

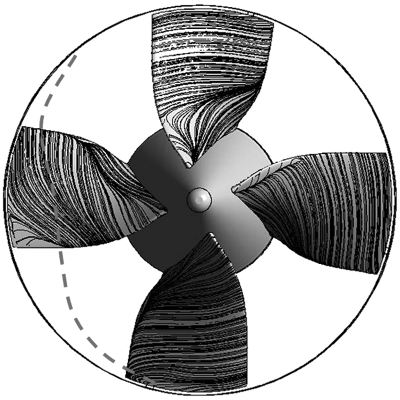

Fig. 12 Surface streamlines on the rotor. The dashed line indicates the region of blade tip stall ($\alpha = 0°$, $U_\infty = 40$ m/s, and $N = 26,200$ rpm; cf. [23]).

Furthermore, the fan inlet features a negative time-averaged radial velocity component in its front part (Fig. 14c), whereas $\bar{v}_r/U_t$ is positive downstream of the hub cap. This distribution of mean radial velocity is induced by a mean streamwise velocity component occurring at the fan inlet (Fig. 14d). Distributions of instantaneous velocity components at $z/t = 0.30$ indicate similar characteristics (Fig. 15).

The circumferential distributions taken at the midspan position (at $z/t = 0.30$, Fig. 10b) of the mean axial, circumferential, and radial velocity components are presented in Fig. 16 and compared to the reference case. The abbreviation REF indicates the velocity component obtained for the reference simulation of the fan alone without distortion. The abbreviation FIW (fan-in-wing) denotes the time-averaged velocity components obtained for the fan-in-wing simulation. The bars shown in Fig. 16 indicate the fluctuation range of the velocity components and of the swirl angle.

The strong velocity gradient occurring above the inlet lip leads to a rise of the time-averaged axial-velocity magnitude $|\bar{v}_a|$ in the front part of the fan inlet section and around the midspan position, compared to the reference without distortion (Fig. 16a). A maximum of $|\bar{v}_a|$ is reached around $\theta = 120°$. A small area of reduced mean axial-velocity magnitude, with respect to the reference value, is present downstream of the hub cap (around $\theta = 0°$). Because of the fan rotation, the axial-velocity component features also a dynamic behavior. Fluctuations of axial velocity are particularly concentrated in the front part of the fan inlet, due to the separation bubble.

Compared to the reference, the magnitude of $\bar{v}_c$ is strongly increased within the region $-30° \le \theta \le 150°$ and is reduced

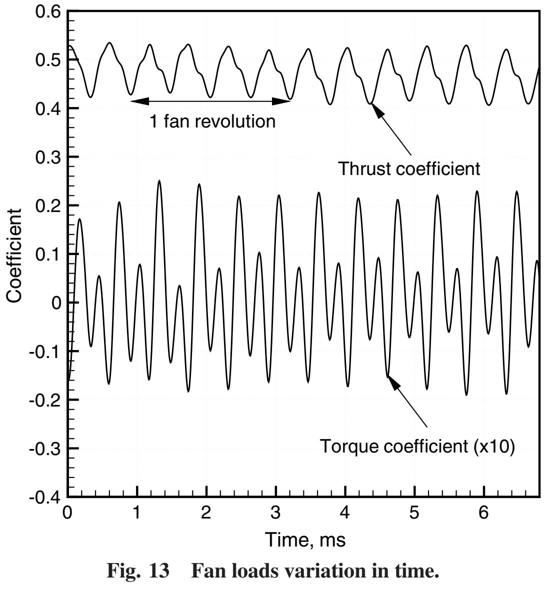

Fig. 13 Fan loads variation in time.

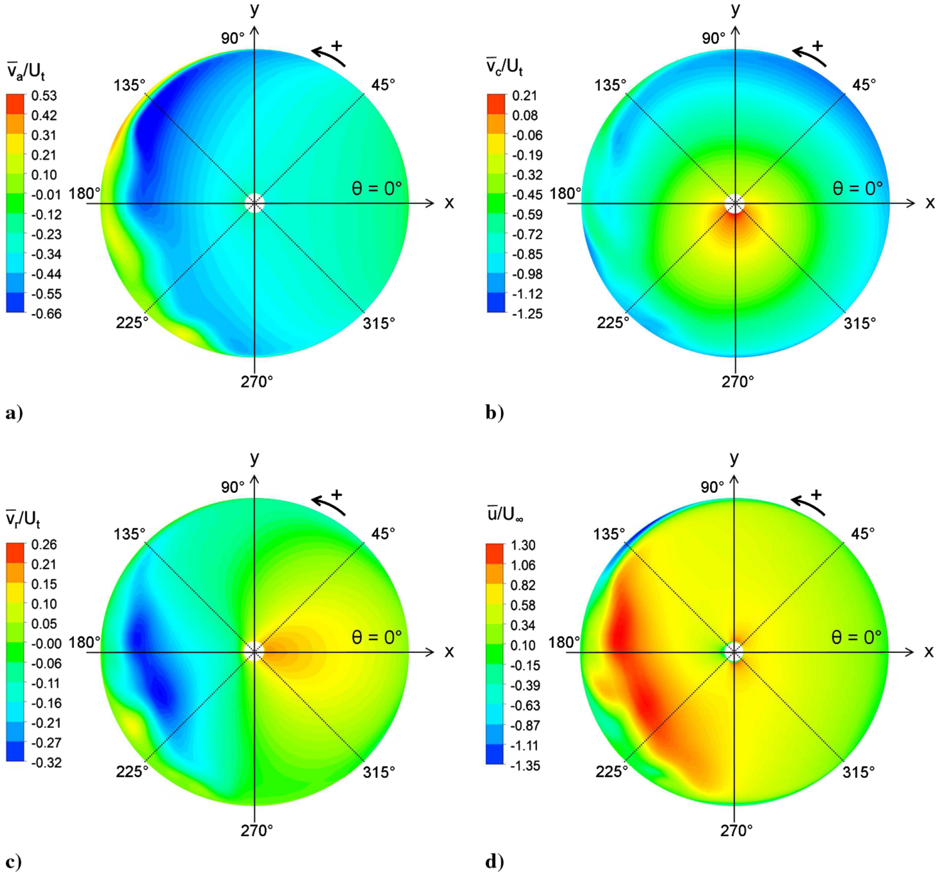

Fig. 14 Distributions of time-averaged a) axial-velocity ratio $\bar{v}_a/U_t$, b) circumferential velocity ratio $\bar{v}_c/U_t$, c) radial velocity ratio $\bar{v}_r/U_t$, and d) streamwise velocity ratio $\bar{u}/U_\infty$ at $z/t = 0.37$ ($U_\infty = 40$ m/s, $N = 26,200$ rpm, and $\alpha = 0°$).

between $180° \leq \theta \leq 300°$ (Fig. 16b). The retreat of the blade results in a decrease of $|\bar{v}_c|$ in the surrounding flow. Contrary to that, an increase of $|\bar{v}_c|$ is observed around the advancing blade. Significant circumferential velocity fluctuations appear, especially between $180° \leq \theta \leq 360°$.

At midspan and compared to the reference, the time-averaged radial velocity component $\bar{v}_r$ decreases significantly in the front part of the fan inlet section (around $\theta = 180°$) and increases downstream of the hub cap (Fig. 16c). Similar to the other velocity components, the fluctuation part of the radial velocity component v_r' varies considerably in the front part of the fan inlet section.

Compared to the reference, the variations in the mean axial and circumferential velocity components have an impact on the mean swirl angle $\bar{\gamma}$ and therefore on the mean blade incidence angle. According to Fig. 16d, the strong increase of the time-averaged axial-velocity magnitude around $\theta = 180°$ results in a significant reduction of the mean swirl angle (spot 2, Fig. 17b) and therefore in a decrease of the incidence angle on the blade. Note that between $-30° \leq \theta \leq 30°$, the mean swirl angle slightly increases, due to an increment of circumferential velocity magnitude (spot 1, Fig. 17a). At this location, the mean axial velocity is comparable to the reference axial velocity. At $\theta = 160°$, the standard deviation of the swirl angle is 12% of the mean value. Circumferentially averaged at midspan, the standard deviation of γ is 6% of the mean value.

To summarize these findings, the wing incoming boundary layer separates on the inlet lip and generates a separation bubble at the fan inlet. Reverse flow is observed on the front part of the shroud. The core of the separation bubble is characterized by low pressure, small axial-velocity magnitude, and therefore large blade incidence, which induces blade tip stall (Fig. 17c). Downstream of the bubble core, the

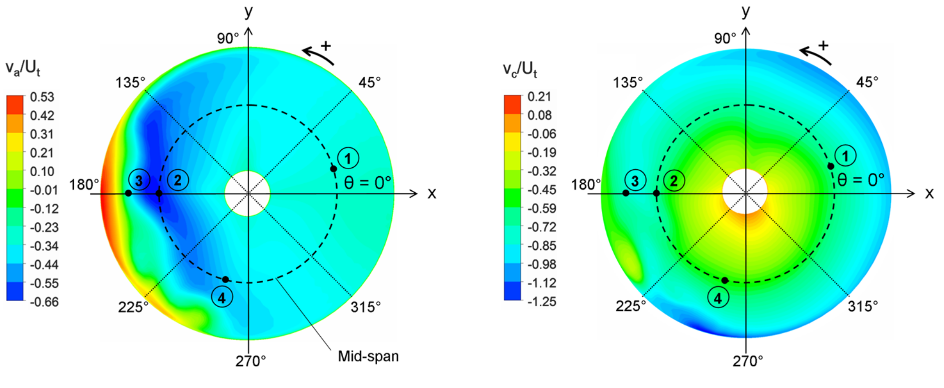

Fig. 15 Distributions of instantaneous a) axial-velocity ratio v_a/U_t and b) circumferential velocity ratio v_c/U_t at $z/t = 0.30$ ($U_\infty = 40$ m/s, $N = 26,200$ rpm, and $\alpha = 0°$).

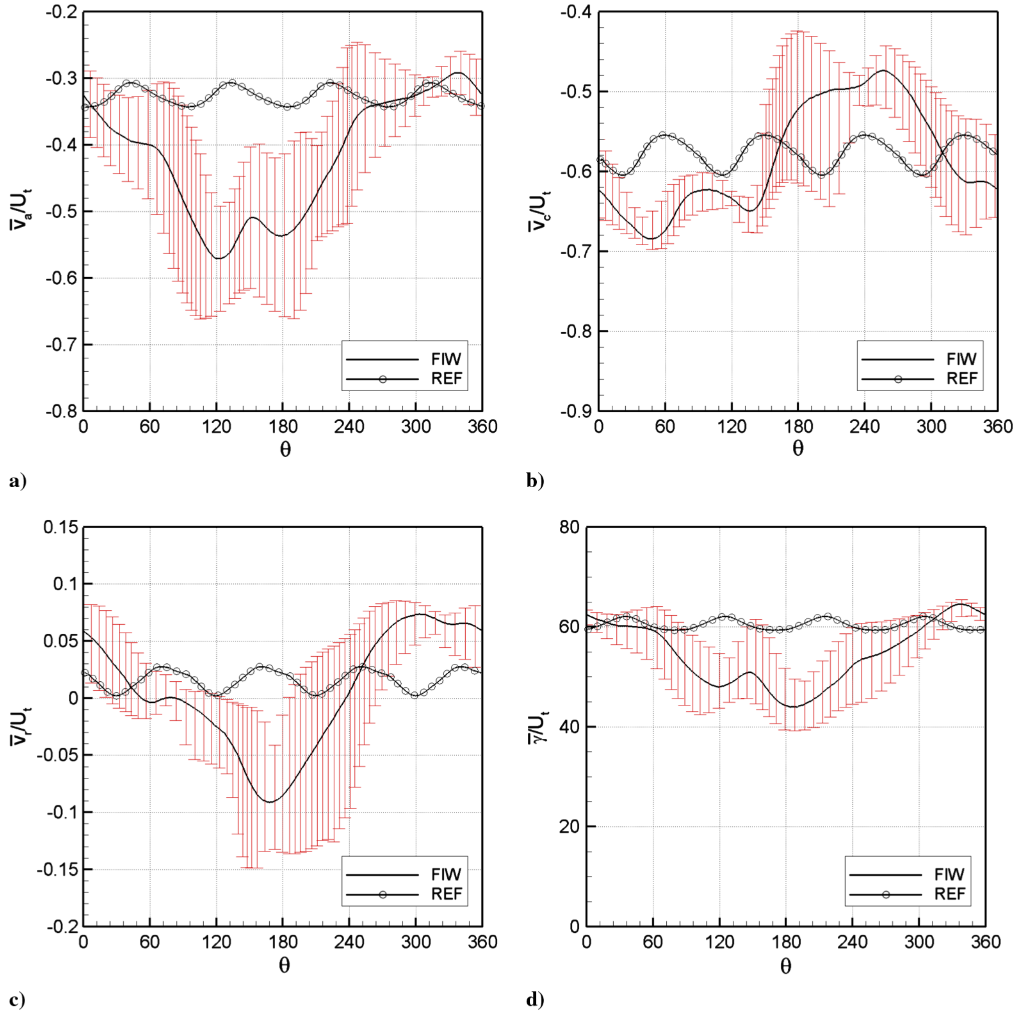

Fig. 16 Circumferential distribution at midspan of time-averaged a) axial-velocity ratio $\bar{v}_a/U_t$, b) circumferential velocity ratio $\bar{v}_c/U_t$, c) radial velocity ratio $\bar{v}_r/U_t$, and d) swirl angle $\bar{\gamma}$ ($z/t = 0.3$, $U_\infty = 40$ m/s, $N = 26,200$ rpm, and $\alpha = 0°$).

magnitude of the axial-velocity component is considerably increased and the blade incidence angle is consequently reduced (Fig. 17b). Compared to the reference, an increase of the circumferential velocity magnitude occurs near the advancing blade, whereas $|v_c|$ (Fig. 17a) decreases in the flow surrounding the retreating blade (Fig. 17d). A qualitative analysis is given in Fig. 18. Note that the blade element passing in the region of strong axial-velocity increase (approximately for $90° < \theta < 270°$ and between 20 to 75% of the span) is subject to a large suction on its upper side. For this reason, a higher loading is observed on this blade thereby generating more thrust than the blade in the region of low total pressure distortion (roughly on the rear part of the inlet section). The static pressure distribution on the blade passing the nondistorted region is similar to the pressure distribution on the blade of the reference calculation. Therefore, the thrust coefficient is larger for the fan-in-wing simulation compared to the reference case.

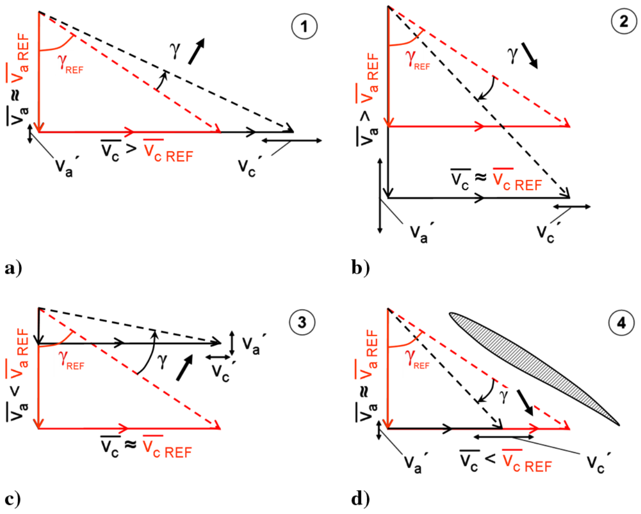

Fig. 17 Flow conditions at the rotor blade at midspan and around a) $\theta = 60°$, b) $\theta = 180°$, c) $\theta = 260°$ and at 75% of the rotor blade span around d) $\theta = 180°$. The position of the spots 1–4 are indicated in Figs. 15 and 18.

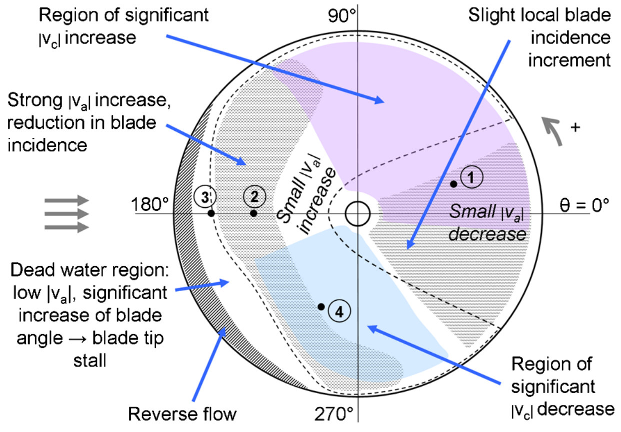

Fig. 18 Sketch of the inlet section velocity distribution.

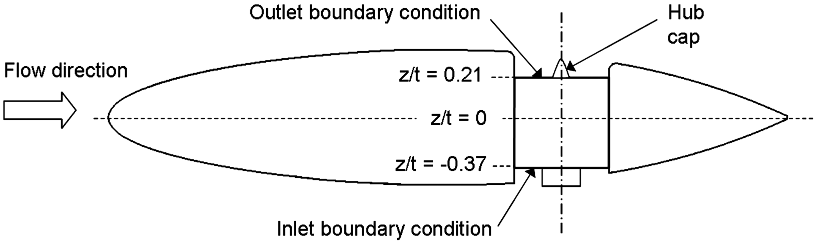

Fig. 19 Schematic view of the actuator disk setup.

III. Inlet Distortion Parameters

Unsteady computations of the entire fan-in-wing configuration require significant computational resources. Replacing the fan by an actuator disk contributes to reduce the computational costs, necessary for a parameter study. The effect of meaningful parameters on the inlet distortion are documented here. The present section refers directly to Sec. II.C. where the distortion characteristics are precisely reported for a particular configuration of fixed parameters.

A. Numerical Method

As sketched in Fig. 19, the fan is removed from the geometry and substituted by boundary conditions at the fan inlet and exit. On the disk upper side (located at $z/t = 0.21$) an outlet boundary condition is imposed with a uniform axial-velocity profile U_j. On the disk lower side (located at $z/t = -0.37$), an inlet boundary condition is set with the same uniform axial-velocity distribution (U_j). For the URANS simulation, the velocity distribution in the cross section $z/t = -0.37$ is studied downstream of the stator. It is shown that most of the swirl component is removed. Therefore, an uniform axial velocity is sufficient on the disk lower side. In the next sections, the inlet distortion is studied in a fan crossflow plane placed at $z/t = 0.3$ (also the investigated cross section above the rotor in the fan-in-wing URANS simulation; cf. Fig.10b). At this location, geometrical modifications induce a variation of the axial-velocity distribution that is not imposed by the uniform axial-velocity boundary prescribed on the disk upper side. The present actuator disk approach is therefore suitable to investigate the inlet distortion caused primarily by the boundary-layer separation occurring on the inlet lip. The turbulence intensity prescribed is 7%, according to the URANS simulation.

A structured mesh is constructed around the geometry. Details of the grid employed are given in Table 4. A grid-dependence study is provided in [24]. Steady Reynolds-averaged Navier–Stokes calculations are conducted using the k-ω SST turbulence model, as in the aforementioned URANS calculations. Identical boundary conditions are imposed on the computational domain (Fig. 7a), as for the fan-in-wing simulation described in Sec. II.B.1. All root-mean-square residuals are converged to less than 1×10^{-5}.

The prediction capability of the actuator disk simulation has been assessed by comparison with experimental data (forces, surface pressures, PIV flowfields, and wool-tuft visualizations) and with the corresponding time-averaged URANS simulations results in [24]. The actuator disk setup gives a good prediction of the mass flow through the fan as well as of the pressure-rise coefficient. Therefore, the flow topology and the pressure distribution on the wing are well represented. In this paper, only circumferential distributions of the mean pressure coefficient are presented in Fig. 5. The actuator disk approach provides a good prediction of C_p around the fan inlet, compared to the experimental data and the time-averaged URANS results.

Table 4 Details of the grid employed for the parameter study

Parameter	Value
Wraparound points	198
Leading-edge spacing/c	3.1×10^{-3}
Trailing-edge spacing/c	5.0×10^{-4}
Inlet-lip spacing/r_{lip}	0.08
Total number of nodes	1.44×10^6

B. Distortion Parameters

The key parameters affecting the lift-fan inlet distortion are documented here to provide additional design sensitivities.

1. *Effect of the Lip Radius-to-Diameter Ratio*

Increasing the value of the inlet-lip radius-to-diameter ratio r_{lip}/D contributes to diminishing the suction peak on the inlet lip and thereby reduces the adverse pressure gradient. Consequently, the relative location (angular position on the lip) of the separation line on the curved inlet is displaced downstream. The spatial extension of the separation bubble is considerably reduced. Thus, increasing r_{lip}/D reduces the total pressure inflow distortion (Fig. 20). The swirl distortion is therefore decreased, due to a lower axial-velocity magnitude in the front part of the inlet section.

A specific inlet-lip design with a variable lip radius remains an alternative to decrease the inflow total pressure distortion. As an example, the inlet lip was modified for a velocity ratio of $U_\infty/U_j = 0.5$. The effect on the total pressure distribution at the inlet and the streamlines on the lip are shown for a constant lip radius (Fig. 21a) and a variable lip radius (Fig. 21b). With a large lip radius-to-diameter ratio of $r_{\text{lip}}/D = 0.35$, flow separation is avoided on the front part of the lip. On each side of the variable lip, a value of $r_{\text{lip}}/D = 0.15$ has been selected. Indeed, for a smaller radius, flow separation can occur on each side of the inlet lip. With this variable lip optimized for $U_\infty/U_j = 0.5$, the lip separation is prevented and the total pressure distortion is considerably reduced. The inlet-lip design is therefore a significant parameter affecting the inlet distortion. However, the retreating and advancing flow condition, due to the fan rotation that affects the flow separation (cf. Sec. II.C.) needs to be considered to design an actual lip. The effect of the retreating and advancing flow conditions would be less significant for a larger inflow depth above the fan.

2. *Effect of the Velocity Ratio*

The velocity ratio U_∞/U_j has a strong influence on the total pressure ratio distribution at the fan inlet. The ratio U_∞/U_j accounts indirectly for the fan rotational speed. A decrease of U_∞/U_j (therefore an increase of the jet velocity and the mass flow through the fan) results in a displacement of the separation line on the front part of the inlet lip. As U_∞/U_j is reduced, the separation point at the fan centerline moves downstream (Fig. 22). Accordingly, the stagnation region on the rear part of the inlet lip is pushed downstream. At higher jet speeds, the stagnation area is located downstream of the inlet lip, causing significant lift penalty on the wing. The size of the separation bubble increases with increasing U_∞/U_j (Fig. 23). The parameter $l_{\max}$ represents the maximum radial extension of the separation bubble measured from the shroud, as indicated in Fig. 23. As the velocity ratio is reduced, the size of the bubble is significantly enhanced. The radial bubble extension characterized by $l_{\max}$ varies almost linearly with respect to the velocity ratio. As the jet velocity decreases, the circumferential extension of the bubble is increased. The total pressure ratio distribution taken at the fan centerline is

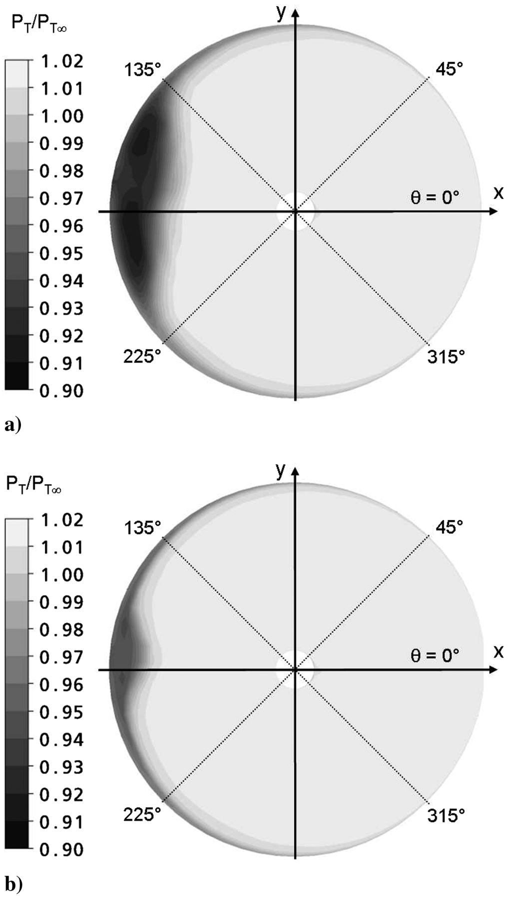

Fig. 20 Total pressure ratio contours at the fan inlet for a) $r_{\mathrm{lip}}/D = 0.083$ and b) $r_{\mathrm{lip}}/D = 0.167$ ($z/t = 0.3$, $U_\infty/U_j = 0.65$, and $\alpha = 0^\circ$).

shown in Fig. 24 and characterizes the inflow pressure distortion. An increase of the mass flow through the fan results in a higher velocity gradient over the inlet lip. Consequently, a larger suction peak is generated in the front part of the fan inlet. Because of the large separation bubble created at high U_∞/U_j, the pressure gradient is reduced from the shroud to the hub. In this case, the major part of the circumferential extension of the flow distortion is contained within $\theta = 135$ to 225°. Summarizing, increasing the jet speed reduces the radial and circumferential extension of the separation bubble. However, the total pressure inflow distortion is locally increased, near the front part of the inlet section, due to a strong suction caused by a large velocity gradient over the inlet lip.

3. *Effect of the Angle of Attack*

A change of the angle of attack has a negligible impact on the total pressure distribution at the fan inlet (as far as the flow remains attached) and for a fan located on the wing rear part. Downstream of its inlet, the fan maintains the flow attached at the trailing edge at $\alpha = 0^\circ$ (Fig. 9). The trailing-edge separation extends upstream as the wing angle of attack is increased. However, no trailing-edge separation is observed in the region downstream of the fan below $\alpha = 20^\circ$ [22]. The radial total pressure distribution (Fig. 25) at the fan middle line confirms this conclusion. The boundary-layer separation on the inlet lip is not affected by a variation of the angle of attack. The radial and circumferential extensions of the separation bubble are consequently similar for all α investigated. The stagnation area located on the rear part of the inlet lip remains also unchanged with respect to a variation of angle of attack. Radial and circumferential velocity distributions at the fan inlet are consequently unchanged. The previous conclusions hold if the wing is not stalled. According to [22], stall occurs at about $\alpha = 26^\circ$, resulting in fan surge.

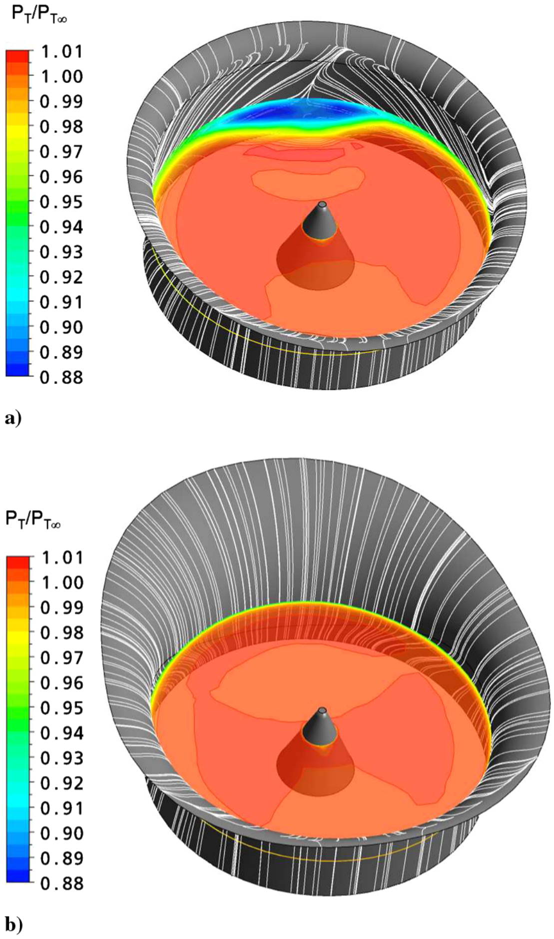

Fig. 21 Total pressure ratio contours at the fan inlet for a) a constant lip radius of $r_{\mathrm{lip}}/D = 0.083$ and b) a variable lip radius of $r_{\mathrm{lip}}/D = 0.35$ in the front part, $r_{\mathrm{lip}}/D = 0.15$ on the sides and $r_{\mathrm{lip}}/D = 0.05$ on the rear part of the inlet lip ($z/t = 0.3$, $U_\infty/U_j = 0.5$, and $\alpha = 0^\circ$).

C. Lip Flow Control via Injection

The design of an inlet lip with variable radius is a passive way of controlling the flow over the lip. The fan has to be housed compactly inside the wing to obtain satisfying cruise performance. Consequently, the value of the lip radius-to-diameter ratio is limited by design constraints. Airfoil flow-control techniques [27] can be applied to the fan inlet to actively control the flow on the lip. These solutions such as blowing or suction can be adjusted to the operating conditions, contrary to a passive lip flow-control approach. In this section, a blown-lip solution is investigated.

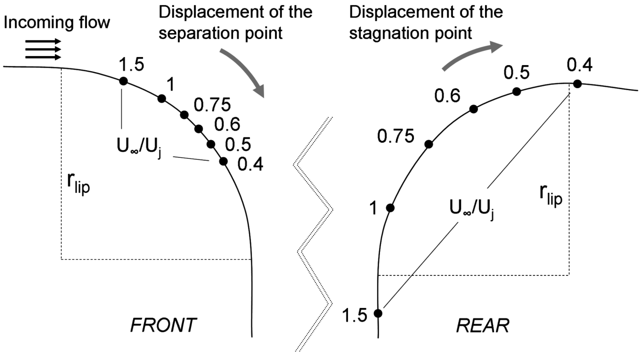

Fig. 22 Relocation of the separation and stagnation point with respect to a decrease of velocity ratio, U_∞/U_j, at the fan centerline ($\alpha = 0^\circ$).

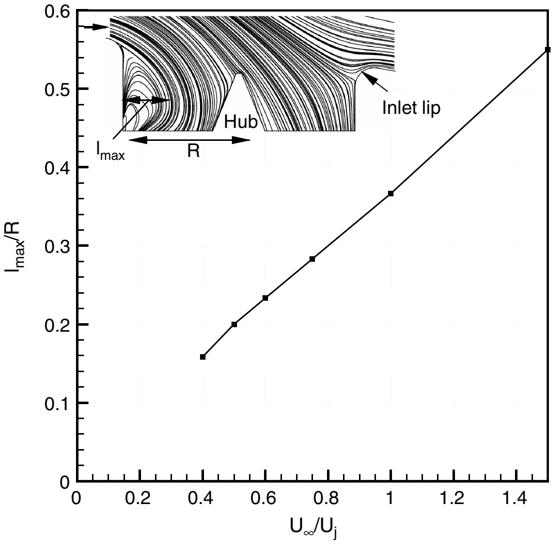

Fig. 23 **Influence of the velocity ratio on radial extension of the lip separation bubble at the fan center ($\alpha = 0°$).**

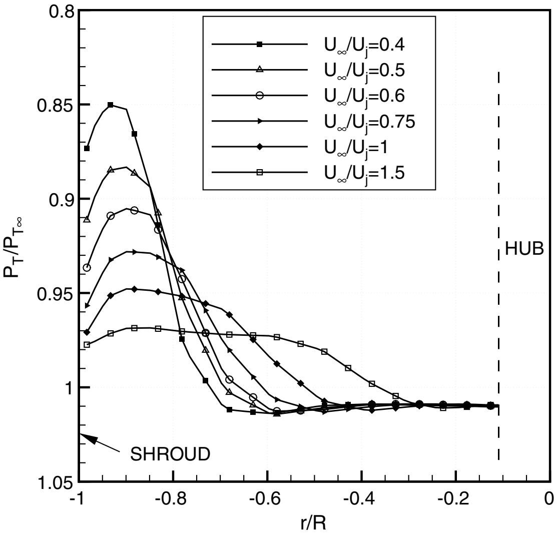

Fig. 24 **Radial distribution of the total pressure ratio $P_T/P_{T\infty}$ at the fan inlet section centerline for various velocity ratios ($z/t = 0.3$ and $\alpha = 0°$).**

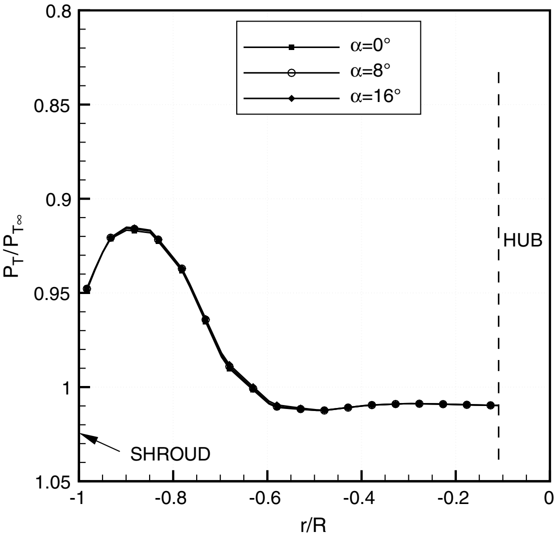

Fig. 25 **Radial distribution of the total pressure ratio $P_T/P_{T\infty}$ at the fan inlet section centerline for various angles of attack ($z/t = 0.3$ and $U_\infty/U_j = 0.65$).**

1. *Setup*

In this section, a constant lip radius of $r_{\text{lip}}/D = 0.083$ is used. A slot of height 0.05 r_{lip} is included in the geometry between the wing and the inlet lip (Fig. 26). The slot extends around the entire fan circumference. As seen previously, lip separation occurs on the front part of the inlet lip. To prevent it, a jet of bulk velocity U_s is blown tangentially to the inlet lip from the slot for $90° < \theta < 270°$. A momentum coefficient is defined in Eq. (1) with respect to the injection operation:

$$C_\mu = \frac{\dot{m}_s U_s}{0.5\rho_\infty V_\infty^2 S} \tag{1}$$

A mesh similar to that in Table 4 is used for the computations. Additional blocks are created near the inlet lip and the shroud to describe the slot inlet face. A slight refinement is performed near the blowing slot, compared to the mesh described in Sec. III.A. Although its value depends on the momentum coefficient, y^+ remains below 2 for all C_μ investigated here. The total number of nodes is about 1.6×10^6.

2. *Results*

Flow separation on the inlet lip can be avoided if the momentum coefficient is sufficient. To enlarge the lip design sensitivity, the minimum C_μ needed to prevent lip separation is presented in Fig. 27 for several velocity ratios. For $U_\infty/U_j > 0.7$, the momentum

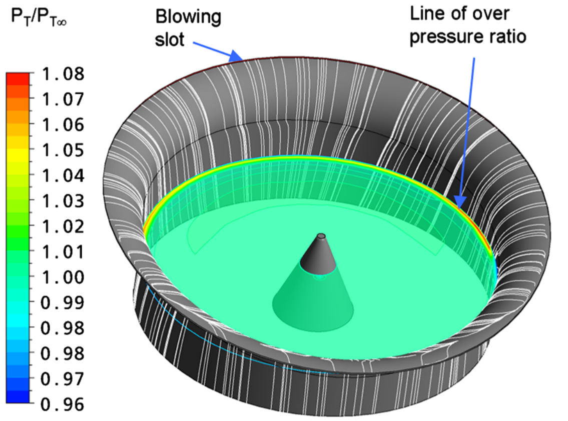

Fig. 26 **Streamlines on the lip and total pressure ratio distribution at the fan inlet ($z/t = 0.3$ and $U_\infty/U_j = 0.5$ and $C_\mu = 8.1 \times 10^{-3}$).**

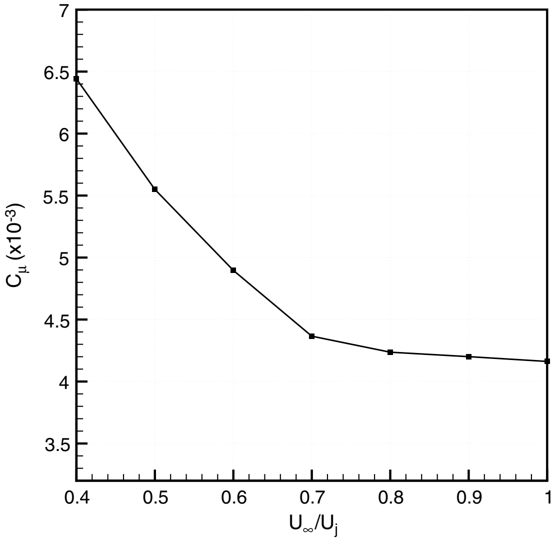

Fig. 27 **Minimum blowing-slot momentum coefficient to maintain attached flow on the inlet lip ($\alpha = 0°$).**

coefficient required remains fairly constant, due to the small change of fan jet velocity. For low-velocity ratios, the momentum coefficient needed increases significantly. However, note that the ratio U_s/U_j decreases linearly as the ratio U_∞/U_j is reduced. Blowing tangentially over the inlet lip can therefore suppress the lip separation. However, an overpressure is induced near the shroud and especially on each side of the fan (Fig. 26). On the front part of inlet lip and without blowing, flow separation occurs upstream (in terms of angular position on the lip) as on the lip sides, due to a more adverse pressure gradient (Fig. 21a). A blown jet of lower momentum coefficient would therefore be sufficient to keep the flow attached on the lip sides. A variable momentum coefficient along the lip can reduce the requirements.

IV. Conclusions

The aerodynamic characteristics of a lift fan under inflow distortions in the form of a generic fan-in-wing configuration have been studied. The total pressure and the velocity distributions at the fan inlet have been analyzed by comparing results of unsteady Reynolds-averaged Navier–Stokes computations using a sliding-mesh approach to steady results of the fan alone without inlet distortion. The main part of inlet distortion originates from the separation of the wing boundary layer on the inlet lip, which generates a separation bubble above the rotor blades. In the front part of the inlet section and around midspan, the axial-velocity magnitude is strongly enhanced, compared to the fan alone without distortion. This results in a decrease of the swirl angle as well as the blade incidence angle. In the bubble core, a low axial-velocity component induces a large local blade incidence angle. Therefore, the rotor is subject to blade tip stall in this region. The dynamic behavior of the distortion impacts significantly on the blade loading.

To extend the design sensitivity of the lift-fan inlet, the main parameters influencing this specific inlet distortion configuration have been documented by means of an actuator disk approach. The main conclusions are as follows:

1) The ratio of the freestream velocity to the jet velocity notably affects the separation on the inlet lip and therefore the total pressure distortion at the fan inlet. Increasing the inlet-lip radius-to-diameter ratio contributes to reduce the pressure gradient on the inlet lip and delays the lip separation, resulting in a less distorted inflow. The design of a lip with variable radius can be a passive lip flow-control solution. The angle of attack on the wing has negligible influence on the total pressure distribution at inlet of a fan located at the rear part of the wing.

2) Blowing a jet over the inlet lip can suppress the boundary-layer separation on the inlet lip, by taking advantage of the Coanda effect. A line of over total pressure is induced, however, at the fan inlet near the shroud and especially on the sides. As the velocity ratio decreases, a higher momentum coefficient is required to maintain attached flow on the lip.

Additional work will be carried out on the design of an inlet lip with variable lip radius, taking into account a retreating and advancing flow conditions, due to the fan rotation. The effect of inlet guide vanes on the fan inflow will be investigated.

Acknowledgments

The authors would like to thank ANSYS, Inc., for providing the flow simulation software CFX and Schübeler Modellsysteme und Antriebstechnik for providing the fan CAD data. The support of these investigations by the Bauhaus Luftfahrt e.V. is gratefully acknowledged.

References

[1] Gologan, C., Heister, C., Kelders, C., Kuhlmann, A., and Seifert, J., "Perspectives of Vertical/Short Take Off and Landing in Commercial Aviation," *Proceedings of the CEAS European Air and Space Conference*, Berlin, 2007.

[2] Nelms, W. P., and Anderson, S. B., "V/STOL Concepts in the United States—Past, Present and Future," NASA TM-85938, April 1984.

[3] Danforth, C. E., "Distortion-Induced Vibration in Fan and Compressor Blading," *Journal of Aircraft*, Vol. 12, No. 4, 1975, pp. 216–225. doi:10.2514/3.59819

[4] Jahren, W., Peters, T., and Fottner, L., "An Experimental Flow Investigation of an HP Five-Stage Compressor Exhibiting Rotating Stall due to Distorted Inlet Flow Conditions," *Unsteady Aerodynamics and Aeroelasticity of Turbomachines*, Kluwer Academic, Dordrecht, The Netherlands, 1998, pp. 243–257.

[5] Hah, C., Rabe, D. C., Sullivan, T. J., and Wadia, A. R., "Effects of Inlet Distortion on the Flow Field in a Transonic Compressor rotor," *Journal of Turbomachinery*, Vol. 120, 1998, pp. 233–246.

[6] Yao, J., Gorrell, S. E., and Wadia, A. R., "A Time-Accurate CFD Analysis of Inlet Distortion Induced Swirl in Multistage Fans," Proceedings of the Joint Propulsion Conference and Exhibit, AIAA Paper 2007-5059, Cincinnati, OH, July 2007.

[7] Jang, C-M., Choi, S-M., and Kim, K-Y., "Effect of Inflow Distortion due to Hub Cap Shape on the Performance of Axial Flow Fan," *Journal of Fluid Science and Technology*, Vol. 3, No. 5, 2008, pp. 598–609. doi:10.1299/jfst.3.598

[8] Hall, C. A., and Hynes, T. P., "Measurements of Intake Separation Hysteresis in a Model Fan and Nacelle Rig," *Journal of Propulsion and Power*, Vol. 22, No. 4, 2006, pp. 872–879. doi:10.2514/1.18644

[9] Podleski, S. D., Smith, C. F., Barankiewicz, W. S., and Zeleznik, S. Z., "Comparison of F/A-18 A Inlet Flow Analysis with Flight Data Part 2," *Journal of Aircraft*, Vol. 33, No. 3, 1996, pp. 463–469. doi:10.2514/3.46967

[10] Potonides, H. C., Cea, R. A., and Nelson, T. F., "Design and Experimental Studies of a Type A V/STOL Inlet," *Journal of Aircraft*, Vol. 16, No. 8, 1979, pp. 543–550. doi:10.2514/3.58562

[11] Sylvester, T., Brown, R., Moore, S., Thorne, G., and Priesley, J., "F-35 STOVL Lift Fan Inlet Development and Lessons Learned," *Proceedings of the International Powered Lift Conference*, London, July 2008.

[12] Krishnappa, G., "Liftting Fan Noise Studies with Superimposed Cross Flows," *Journal of Aircraft*, Vol. 9, No. 10, 1972, pp. 719–725. doi:10.2514/3.59069

[13] Lieblein, S., Yuska, J. A., and Diedrich, J. H., "Performance Characteristics of a Model VTOL Lift Fan in Crossflow," *Journal of Aircraft*, Vol. 10, No. 3, 1973, pp. 131–136. doi:10.2514/3.44357

[14] Schaub, U. W., "Experimental Investigation of Flow Distortion in Fan-in-Wing Inlets," *Journal of Aircraft*, Vol. 5, No. 5, 1968, pp. 473–478. doi:10.2514/3.43969

[15] Kirk, J. V., Hickey, D. H., and Hall, L. P., "Aerodynamic Characteristics of a Full-Scale Fan-in-Wing Model Including Results in Ground Effect with Nose-Fan Pitch Control," NASA TN D-2368, July 1964.

[16] Kirby, R. H., and Chambers, J. R., "Flight Investigation of Dynamic Stability and Control Characteristics of a 0.18-Scale Model of a Fan-in-Wing VTOL Airplane," NASA TN D-3412, USA, 1966.

[17] Hodder, B. K., Kirk, J. V., and Hall, L. P., "Aerodynamic Characteristics of Large-Scale Model with a Lift-Fan Mounted in a 5-percent-thick Triangular Wing, Including the Effects of BLC on the Lift-Fan Inlet," NASA TN D-7031, Dec. 1970.

[18] Hickey, D. H., and Ellis, D. R., "Wind-Tunnel tests of a Semispan Wing with a Fan Rotating in the Plane of the Wing," NASA TN D-88, Oct. 1959.

[19] Gregory, N., and Love, E. A., "Wind Tunnel Tests on a Nacelle Fitted with Two Lifting Fans in Tandem," Aeronautical Research Council, Reports and Memoranda No. 3494, London, 1967.

[20] Kirk, J. V., and Barrack, J. P., "Reingestion Characteristics and Inlet Flow Distortion of V/STOL Lift-Engine Fighter Configuration," *Journal of Aircraft*, Vol. 6, No. 2, 1969, pp. 116–122. doi:10.2514/3.44017

[21] Soranna, F., Chow, Y-C., Uzol, O., and Katz, J., "The Effect of Inlet Guide Vanes Wake Impingement on the Flow Structure and Turbulence around a Rotor Blade," *Journal of Turbomachinery*, Vol. 128, 2006, pp. 82–95. doi:10.1115/1.2098755

[22] Thouault, N., Breitsamter, C., Adams, N. A., Gologan, C., and Seifert, J., "Experimental Investigation of the Aerodynamic Characteristics of Generic Fan-in-Wing Configurations," *The Aeronautical Journal*, Vol. 113, No. 1139, 2009, p. 3338.

[23] Thouault, N., Breitsamter, C., and Adams, N. A., "Numerical and Experimental Analysis of a Generic Fan-in-Wing Configuration," *Journal of Aircraft*, Vol. 46, No. 2, 2009, pp. 656–666. doi:10.2514/1.39750

[24] Thouault, N., Breitsamter, C., Gologan, C., and Adams, N. A., "Numerical Analysis of Design Parameters for a Generic Fan-in-Wing Configuration," *Aerospace Science and Technology*, Vol. 14, No. 1, 2010, pp. 65–77.
doi:10.1016/j.ast.2009.10.004

[25] *CFX-Solver Theory Guide, Release 11.0*, ANSYS, Inc., Canonsburg, PA, Dec. 2006, pp. 119–121.

[26] Menter, F. R., "Two-Equation Eddy-Viscosity Turbulence Models for Engineering Applications," *AIAA Journal*, Vol. 32, 1994, pp. 1598–1605.
doi:10.2514/3.12149

[27] Chng, T. L., Rachman, H. M., Tsai, H. M., and Zha, G.-C., "Flow Control of an Airfoil via Injection and Suction," *Journal of Aircraft*, Vol. 46, No. 1, 2009, pp. 291–300.
doi:10.2514/1.38394

F. Liu
Associate Editor